

# TABLE OF CONTENTS

	Page
Chapter 1: Introduction . . . . .	1
1.1 Motivations for study of WDM . . . . .	4
1.2 Experimental Generation of WDM . . . . .	7
1.3 X-ray diagnostics of WDM . . . . .	10
1.4 Dissertation Outline . . . . .	19
Chapter 2: Physics of PENELOPE . . . . .	20
2.1 Types of interactions . . . . .	20
2.2 Inelastic scattering . . . . .	26
2.3 Accuracy and useful regimes . . . . .	30
2.4 Inelastic scattering . . . . .	33
2.5 Dosimetry . . . . .	34
Chapter 3: X-ray Free Electron Laser-Based Studies of WDM . . . . .	36
3.1 X-ray Free Electron Lasers . . . . .	36
3.2 HED physics at XFEL facilities . . . . .	39
3.3 Scientific Directions . . . . .	40
3.4 Design of an XFEL heating experiment . . . . .	41
3.5 Experimental Work . . . . .	42

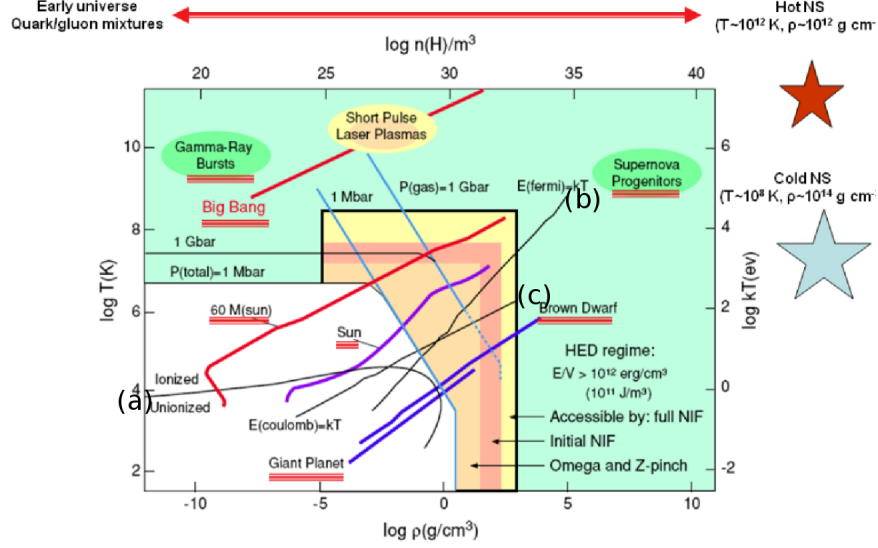
## Chapter 1

### INTRODUCTION

In this thesis I introduce the development of new techniques for the production of materials in the warm dense matter (WDM) regime, and for interrogation of the structure and thermodynamic state of such systems using x-ray diffraction and (to a lesser extent) spectroscopy. The main results include a scheme for single-shot determination of the static structure factors of WDM systems generated at laser plasma facilities; a technique for enhancing the density of deposited energy in WDM generated at fourth-generation X-ray sources such as the Linac Coherent Light Source (LCLS); and interpretation of experimental data that puts new constraints on the thermalization (both electronic and lattice) of a solid state material upon fs-scale XFEL heating. In addition to this thread of research I discuss some secondary work on the development of software and electronics for energy- and position-sensitive pixel detectors including current applications in the context of soft x-ray laboratory and possible future ones in XFEL, synchrotron, and laser plasma facility-based experiments.

Before proceeding it is useful to define WDM in terms of the microphysical context it occupies. Fig. (which figure) presents a map of thermodynamic parameter space, with the logarithm of density and temperature on the horizontal and vertical axes, respectively. A few bounding curves can be identified. First, ionization occurs at temperatures exceeding approximately 1 eV; this is denoted by curve (a), which forms a boundary between the plasma and condensed matter regimes. Second, curve (b) indicates the boundary at which the Fermi energy is approximately equal to the average thermal energy  $k_B T$ ; i.e. where the electron degeneracy parameter,  $E_f/k_B T$  is of order unity. Third, curve (c) corresponds to a value of 1 for the ratio of the Coulomb energy to the thermal one, also called the plasma coupling parameter  $\Gamma$ .

Figure 1.1: The atlas of high-energy density physics (cite)



Above curves (a), (b) and (c) is the regime of classical plasma physics where, as a result of the weak interaction between neighboring ions ( $\Gamma \ll 1$ ), collective interactions predominate over binary collisions and quantum statistics can be neglected ( $\Lambda \ll 1$ ) except for the purpose of calculating blackbody spectra. In this regime continuous, classical modeling treatments are widely-used and fully validated (cites). Below curves (a), (b), and (c) is the low-temperature, intermediate-density realm of condensed matter physics, where the established theoretical framework is that of many-body quantum mechanics, wherein the potential landscape is built on the interaction between electrons and ion cores. In this framework finite-temperature effects are incorporated perturbatively. WDM occupies the transitional regime above curve (a) and near the intersection of curves (b) and (c), characterized by partial degeneracy and strong ion-ion coupling ( $\Gamma$  and  $\Lambda$  of order unity). As a result, treatments of plasma physics originating in the classical regime are not applicable to WDM. Solid state physics models similarly fail in the WDM regime due to large, non-perturbative effects of finite temperature on the structure and thermodynamics of WDM (cites).

Modeling of the ionization potential depression (IPD) in a plasma is a case in point of the difficulties that manifest themselves with theoretical treatments of WDM. Adequate descriptions of IPD are given the Debye-Hueckel approximation and ion sphere model, which cover opposite regimes of high temperature and low density, and low density and high temperature, respectively. We here briefly introduce both model, with focus on the assumptions and approximations that they adopt.

The Debye-Hueckel model applies to a weakly-coupled plasma in local thermal equilibrium. It identifies the electrostatic potential in the Poisson equation with the mean field generated by a population of Maxwell-Boltzmann-distributed ions or electrolytes. This results in the Poisson-Boltzmann equation which, when solved, gives the electrostatic potential produced by an arbitrary charge distribution. The condition for validity of the Debye-Hueckel model is for the Thomas-Fermi screening length (also called the Debye length) to be much larger than the mean inter-ion separation. This condition is satisfied at comparable temperatures, but lower densities, than those encompassed by the WDM regime. (check that this is right, and cite)

In the opposite limit, the ion-sphere model describes IPD in a high-density material with  $\Gamma > 1$  (in the low-temperature context IPD is more commonly referred to as pressure ionization). The picture offered by the ion-sphere model is that of a plasma with highly-correlated ion positions and therefore no close encounters between ion pairs. Each ion is treated as a sphere whose potential is unaffected by the presence of neighboring ions. (cite Stewart-Pyatt). The sphere radius is  $R_0 = (3/4\pi N_i)^{1/3}$ , where  $N_i$  is ion number density, while the orbital radius of the ion sphere's  $n$ th principal energy level is approximately  $r_n = (n^2/Z_n)(0.529\text{\AA})$ . For the  $n$ th bound state to exist it is necessary that  $r_n \leq R_0$ ; thus, IPD manifests itself as a reduction in the number of bound states as a function of the inter-ion distance  $R_0$ . It should be noted that, although the ion-sphere model is a frequently-used heuristic in high-temperature plasmas with near-ambient densities, it is known to be incorrect in the high-density, moderate-temperature ( $\Gamma \gg 1$ ) regime. Neaton et al. have done ab-initio (DFT) simulation of Li—a free electron-like material under ambient conditions—showing

that, contrary to intuitive expectations and the ion-sphere model, it becomes less free-electron like at high densities and additionally loses its common bcc crystal structure. (cite Neaton 1999) Due to overlap of core electrons, the treatment of electronic wavefunctions in this regime is necessarily strongly nonperturbative—again in conflict with the ion-sphere model’s assumptions.

Leaving aside, momentarily, the ion sphere model’s limitations, we might contemplate constructing a model of ionization potential depression that reduces to the ion sphere and Debye-Hueckel models in their respective limits. Doing so is challenging because it allows none of the simplifying approximations invoked by the two limiting cases. One manifestation of uncertainty of the correct approach is the existence of two mutually-contradictory models for IPD in WDM, those of Stewart and Pyatt (cite) and Ecker and Kroll (cite). Though the Stewart-Pyatt model is more widely used and has the virtue of reproducing the ion-sphere and Debye-Hueckel behaviors (cite Crowley review article), its validity has been called into question by recent direct XFEL-measurements of IPD in Al heated to 180 eV (cite Ciricosta paper). Such conflicts exemplify the persistent difficulty of constructing models with validity accross different sub-regimes of WDM.

## ***1.1 Motivations for study of WDM***

In addition to the basic physics questions intrinsic to the WDM regime, there are a number of points of contact between WDM and particular problems in other fields. This interaction has been bolstered in recent years by rapid development of laser plasma facilities and x-ray free electron lasers (XFELs) with unprecedented experimental capability for producing WDM and probing its physical properties. This has brought many previously-intractable physical regimes into the scope of both empirical investigation and numerical simulation.

### *1.1.1 Astrophysical modeling*

A large contribution to this growth in interest is the relevance of WDM theory as a micro-physical basis on for models of various systems in planetary and stellar astrophysics. Here

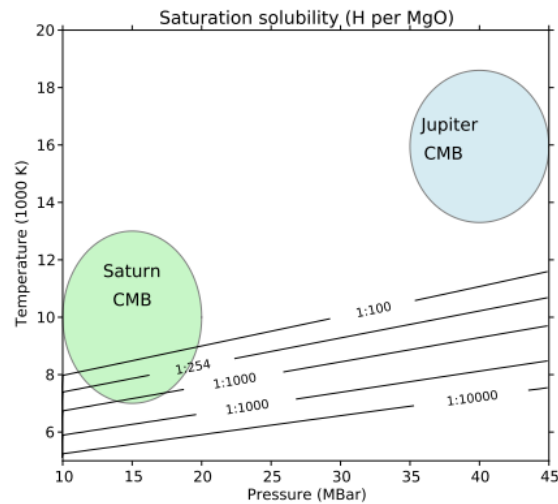
we introduce two examples in which this relationship is salient.

The interiors of both rocky and gas giant planets contain dense, and in some cases Fermi-degenerate, plasmas at 1 eV-scale temperatures. Examples include the iron under conditions of the earth’s core (pressure = 3 Mbar;  $T = 6000$  K), whose viscosity and equation of state (EOS) has consequences on convective heat transfer and the formation of earth’s magnetic field. (cites) Similarly, modeling of the evolution and structure of gas giant planets depends on the EOS of H under the regime of gas giant interiors. The existence of metallic H caused by pressure ionization at Mbar-scale pressures has been experimentally demonstrated, but its onset is poorly understood at the level of theoretical models for the EOS: although a first-order dielectric-to-metal phase transition has been postulated, current approaches do not attempt to model pressure ionization, instead limiting themselves to interpolation between the better-understood atomic and fully ionized limits. (cites)

The solubility physics of two-component WDM mixtures containing H with other species found in rocky planetary bodies has direct consequences on mass transport accross the core-mantle boundary in gas giant planets. It also has crucial importance in the modeling of gas giant formation, where the solubility of H with rocky elements bears on the plausibility of the planetesimal accretion hypothesis for gas gian genesis, which requires condensation of H and He around a rocky core. (cite Wilson MgO solubility paper).

Another case in which the material properties of warm dense matter determine the behavior of an astrophysical object is that of white dwarves, whose envelopes consist of a hot, partially Fermi-degenerate plasma. Modeling the cooling of white dwarves is a topic of interest (cites), especially in the context of the importance of type 1a supernovae as ‘standard candles’ for measuring distances to distant galaxies. Doing so, however, requires knowledge of stellar envelope opacities, equations of state (EOS), and transport properties, many of which properties are currently unknown to within factors of order unity. The absence of understanding of the simplest available system—the hydrogenic one-component plasma—underscores the difficulty of this thread of research.

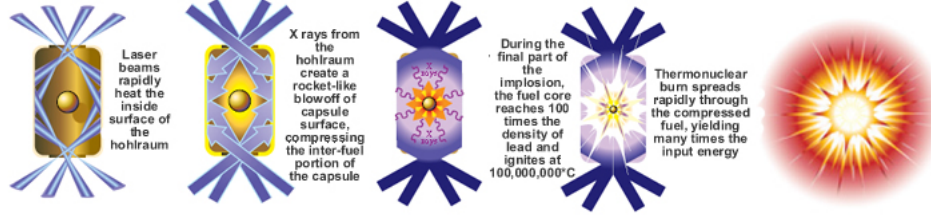
Figure 1.2: Saturation solubility of MgO in H as a function of pressure and temperature from *ab initio* calculation by Wilson et al. The temperature conditions of the core-mantle boundaries of Saturn and Jupiter are indicated. (cite Wilson)



### 1.1.2 Inertial Confinement Fusion

The effort to reach controlled fusion through implosion of deuterium-tritium fuel capsules—an approach termed inertial confinement fusion—has progressed significantly in the last decade due to completion of laboratory facilities capable of producing HED (definition?) plasmas with densities and temperatures approaching levels needed for ignition. Fig. (which figure) shows a schematic of an ignition technique called indirect drive. In this configuration the ICF target, which consists of a hollow spherical capsule of ablator material filled with deuterium-tritium fuel, is confined in a hollow capsule of a high-Z material (the Hohlraum). A multi-TW, ns-duration laser passes through apertures in the Hohlraum and heats the Hohlraum to blackbody temperatures on the order of several hundred eV. The resulting thermal spectrum of soft X rays isotropically heats and ablates the fuel capsule's surface, causing its interior to implode by conservation of momentum. Typical parameters of the plasma created at maximum compression include areal densities (capsule density x radius) of  $0.3 \text{ g/cm}^2$  and temperatures of the order 10 keV. (cite. see x-games pg 113)

Figure 1.3: Schematic of indirect-drive inertial confinement fusion shot. (cite)



Although its end state falls well within the regime of a classical plasma, the fuel capsule transitions through the WDM state during compression. The opacity and EOS of warm dense matter therefore has a strong influence on the development and propagation of shocks during ablation of the fuel capsule, which in turn affects the optimization of various experimental parameters, including fuel capsule geometry and temporal profile of the laser driver. Accurate modeling of the fuel capsule's transport properties under the WDM regime is equally important for understanding the development during compression of hydrodynamic instabilities, which are known to be a major obstacle to the efficient coupling of laser energy into fuel compression (cites).

## 1.2 Experimental Generation of WDM

WDM conditions may be generated using X-ray free electron lasers (XFELs) and several varieties of lasers, found both in large-scale facilities and laboratory-scale systems. Here we provide an overview of existing technologies.

### 1.2.1 Long-pulse lasers

Lasers with pulse durations on the order of nanoseconds and energies of 1 kJ or more are among the most versatile tools for producing high energy density states, including warm dense matter. In the most common use cases of long pulse lasers the target is a bulk material, and coupling of laser energy into it occurs in two stages. First, the laser rapidly (TODO how rapidly) generates a coronal plasma at the material's surface. Once the electron



density of this plasma exceeds the laser wavelength’s critical density (TODO: equation) the laser becomes electromagnetically shielded from the material’s interior and can no longer transfer energy to it. In the context of direct drive (where the material is a target to which laser energy is directly coupled), subsequent energy transfer occurs by thermal conduction of energy from the surface plasma to higher-density regions as well as by compression of the target resulting from ablation of its surface. In the case of indirect drive, the laser’s energy is used to heat a surface (typically the interior of a Hohlraum) that provides a thermal bath which, in turn, couples to the target via its blackbody radiation.

The ns duration of long-pulse lasers matches the timescale on which mechanical and hydrodynamic processes occur on typical target scales. Long-pulse lasers are thus suited to generating ramp and shock compression, notably including for the application of ICF. The largest-scale laser plasma facilities—Omega EP at the Laboratory for Laser Energetics in Rochester, NY and the National Ignition Facility—are long-pulse laser systems targeted toward the ICF program.

### 1.2.2 *Short-pulse lasers*

Short pulse lasers are a second class of systems used to generate HED conditions. They are typically defined by pulse durations on the order of a picosecond or less, down to as little as  $\sim 1$  fs.

Short-pulse laser systems arose after the development of chirped pulse amplification in the 1980s (cite) and have proliferated ever since (cites), especially with the recent advent of compact (university laboratory-scale) versions with tens of Joules of pulse energy, sufficient to generate scientifically interesting HED conditions. The largest-scale short pulse lasers have pulse powers up to 100 TW (check this number), with durations between 10 and 100 fs (check this as well).

Due to the smaller total energies of short-pulse lasers and the relatively slow cooling timescale of materials heated above ambient conditions *regardless* of the pump duration, short-pulse lasers are used to generate HED conditions under direct-drive configurations

alone. Energy is coupled into a target indirectly (as is the case with long-pulse systems) via ‘hot’ MeV-scale electrons generated in the laser’s interaction with plasma at the target surface. In the (typical) case where bulk heating is required, the target thickness is small compared to the hot electrons’ stopping range, causing them to reflux through the target once it acquires net positive charge. This process lasts on the order of one ps (check this, cite Nilson and maybe others) and thus sets the time resolution of experiments in which the short-pulse laser is used to both heat and probe the target.

### *1.2.3 X-Ray Free Electron Lasers*

The advent of X-Ray Free Electron lasers is a major advance in capability for WDM research. Existing incarnations of these sources, notably the Linac Coherent Light Source (LCLS), provide  $10^{14}$  photons in a  $\geq 10$  fs-duration monochromatic pulses with tunable energy. While the energies per pulse are smaller than those attainable with a short-pulse laser, they are largely sufficient to produce HED states with temperatures in excess of 100 eV (cite). Because XFELs can heat volumetrically, they are free of the primary deficiency of lasers with respect to the task of generating dense plasmas: namely, the latter can only heat bulk materials indirectly and over durations of 1 ps or longer, which exceeds the timescale for changes in WDM, preventing the study of short-lived transient states.

The ability to generate (and probe) WDM on truly inertial timescales, wherein atomic nuclei are effectively frozen, has been duly exploited in early pioneering studies at the LCLS. It forms the basis, for example, for a new thread of materials science research on nonthermal lattice and spin dynamics (cite Lee and others). Likely even more significantly, it is the enabling feature for macromolecular crystallography under the ‘diffract before destroy’ paradigm. (cites) The possibilities surrounding rapid generation of WDM is a topic to which I return in (which chapter?). (cite Vinko et al. and other early LCLS papers).

### 1.3 X-ray diagnostics of WDM

Experimental studies of WDM suffer from a substantial complication: the opacity of WDM to photons is large at energies up to the soft X ray regime. As mentioned in section 1.2.2, in the context of laser heating this is merely a frustration; for the purposes of measuring the conditions of a bulk WDM system, however, the need for direct detection of radiation originating from the target's interior makes optical probes wholly ineffective. Determination of the structure and thermodynamic state variables of a dense plasma therefore requires sufficiently penetrating radiation; for this reason, the large majority of WDM diagnostics are X ray photon-in photon-out measurements.

In the remainder of this section I provide an overview of the various available X-ray techniques.

#### 1.3.1 Scattering

Elastic scattering and nonresonant inelastic X-ray scattering (NIXS) are among the most-frequently probed signals for inferring the structure, temperature and ionization state of WDM. In dense plasmas generated by long-pulse lasers, where LTE is commonly assumed, NIXS also serves as a probe of temperature.

For a given sample, the sum of scattering interactions is characterized by the double-differential scattering cross section (DDCS)  $d^2\sigma/d\Omega d\omega$ , which describes the probability of a photon to scatter into a solid angle increment  $d\Omega$  within an energy loss interval  $d\omega$ . Within the independent-electron and first Born approximations the DDCS is given by

$$\frac{d^2\sigma}{d\Omega d\omega} = r_0^2 \left(\frac{\omega_2}{\omega_1}\right) |\epsilon_1 \times \epsilon_2^*|^2 S(\vec{q}, \omega), \quad (1.1)$$

where

$$S(\vec{q}, \omega) \equiv \sum_F \sum_j \langle F | \exp(i\vec{q} \cdot \vec{r}_j) | I \rangle|^2 \delta(E_F - E_I - \hbar\omega). \quad (1.2)$$

The first term in equation 1.3.1 is the Thomson cross section, which describes the interaction between a probe photon and a single electron;  $S(\vec{q}, \omega)$  is referred to as the dynamic structure factor, and encapsulates all system-specific properties.  $I$  and  $F$  are initial and final states of the sample with energies  $E_I$  and  $E_F$ , respectively, and the second summation of 1.3.1 is over electrons in the scatterer.

Following Chihara (cite Chihara), the typical treatment of a dense plasma separates the dynamic structure factor into several components:

$$S(\vec{q}, \omega) = |f_I(q) + f_e(q)|^2 S_{ii}(q, \omega) + S_{ff}(q, \omega) + S_{bf}(q, \omega), \quad (1.3)$$

$S_{ii}$  is the atomic/ionic structure factor,  $f_I$  and  $f_e$  are the form factors for the ion and a surrounding cloud of screening charge.  $S_{ff}$  contains scattering from free, delocalized electrons, and  $S_{bf}$  represents Raman-type bound-free transitions resulting from scattering from tightly-bound core level electrons. Note that spherical symmetry has been assumed: all terms of the structure factor depend only on the magnitude of  $\vec{q}$ .

The first term corresponds to elastic ( $\omega = 0$ ) scattering, and is connected to the dense plasma's pair distribution function by a Fourier transform. Though not a component of the NIXS signal, it must often be considered in simulations and analyses of NIXS data, wherein the Bethe sum rule (cite) and other conserved quantities consist of integrals over the entire energy-loss domain of the dynamic structure factor. Elastic scattering is a highly-useful probe of structure; we consider it separately in section 1.3.1.

The free-free contribution to  $S(q, \omega)$  can be expressed in terms of the free-electron dielectric function  $\epsilon(q, \omega)$  via the fluctuation-dissipation theorem (cite Kubo et al.):

$$S(q, \omega) = \frac{\epsilon_0 \hbar q^2}{\pi e^2 n_e} \frac{1}{1 - e^{\hbar\omega/k_B T_e}} \text{Im} \frac{1}{\epsilon(q, \omega)}, \quad (1.4)$$

The random phase approximation (RPA) (cite Bohm and Pines) is typically used as an approximation for  $\epsilon(q, \omega)$ , but more recent treatments incorporate a perturbative treatment of electron-ion interactions using the Born-Mermin Approximation (cite Mermin). As shown

in Fig. (which figure?), the scattering contribution of  $S_{ff}$  consists of a pair of Plasmon peaks with opposite, equal-magnitude energy offsets from the elastic scattering peak. Electron density is inferred from the magnitude of the Plasmon peak shifts while temperature is obtained from the ratio of intensities of the two peaks, following the principle of detailed balance (cite Glenzer 2007 and Lee 2009).

Although the connection of temperature and density to the free-free component of the dielectric function is well-founded, there are two obstacles to effective interpretation of collective scattering data from WDM systems; one is theoretical and the other experimental. First, the validity of established treatments of the dielectric function has been called into question, with recent plasmon spectrum calculations based on MD-DFT simulations showing a significant change in the plasmon profile compared to that predicted by the BMA. (cite Mattern thesis and Plagemann). Second, the plasmon peak suffers from poor signal to background and has a small separation from the elastic scattering peak under typical WDM electron densities, making it difficult to resolve. As a result only a handful of experiments to date have pursued this technique.

We finally turn our attention to the last term of 1.3.1,  $S_{bf}$ , whose contribution to the inelastic DDCS is often referred to as x-ray Thomson scattering (XRTS). Obtaining state variable information from a system's bound-free scattering contribution is dependent on the underlying model of electronic structure used; as a result, various treatments exist, including the Impulse Approximation (IA) of Eisenberger and Platzman, wherein the bound-free contribution to XRTS is equivalent to Doppler-broadened Compton scattering (cite Eisenberger and Platzman); the plane wave form factor approximation (PWFFA) of Schumacher (cite Schumacher), which attempts to extend the IA by incorporating electron binding energies; and calculation of matrix elements using a real space Green's function (RSGF) formalism applied to atomic clusters, as implemented in the atomic spectroscopy code FEFF (cite Mattern).

In current practice, measurement of the bound-free component of XRTS from WDM is performed in the large- $q$  regime, where the Compton feature is broad and can be measured

using high-efficiency (but low-resolution) HOPG-based spectrometers (need cites for this). As such, single-particle bound-free scattering is more readily measured than collective excitation features. Since an early demonstration of the technique by Glenzer et al. (cite Glenzer 2003) it has been frequently implemented at both laser plasma and XFEL facilities (cite figures showing how these experiments are set up). Despite some fruitful outcomes (how so? need examples, cites), the large statistical uncertainties in XRTS spectra—particularly at laser plasma facilities, where single-shot measurements are photon-starved—make the inference of state variables difficult, and dependent on one’s choice of electronic structure model (check that this is right. do predicitions heavily depend on the choice of model, or is it just that uncertainties are high, regardless of the choice?). Mattern et al. have demonstrated this concretely by comparing theoretical fits to XRTS data of shock-compressed Be, and argue that the lack of rigorous validation of electronic structure models for WDM models strongly undermines their validity for first-principles measurement of state variables. With this context as motivation, we revisit the topic of WDM thermometry in chapter (reference chapter).

### 1.3.2 *Coherent Scattering*

Coherent scattering is the zero-energy loss component of the double differential cross section. The inference of structural information from coherent scattering varies by material; two primary cases present themselves.

First, for amorphous materials, such as hot dense plasmas generated by ramp- or shock-compression and lacking long-range order, the scattering amplitude is isotropic and is characterized by the one-dimensional static structure factor, which is connected by a Fourier transform to the material’s pair correlation function. Inference of the full pair correlation function is in practice frustrated by the difficulty of inverting a limited momentum transfer range-sampling of the strucure factor, but even in the most information-limited scenarios a density can nevertheless be recovered from the strucure factor’s first correlation peak. Although coherent scattering measurements from dense plasmas have been demonstrated in

the context of long-pulse laser compression experiments, implementation difficulties unique to that environment prevent its adoption as a routine technique. We address these difficulties, and proposed solutions, in chapter (chapter reference). (cite Ma et al).

Second, in materials with long-range crystalline order, as typically found in XFEL-based experiments (whose timescales are shorter than the thermalization rate of electronic and ionic degrees of freedom), the coherent scattering amplitude is given by

$$F(\vec{q}) = \sum_n e^{i\vec{q} \cdot \vec{R}_n} \sum_j f_j(\vec{q}) e^{i\vec{q} \cdot \vec{r}_j}, \quad (1.5)$$

where the first summation is over all lattice vectors  $\vec{R}_n$  and the second, referred to as the *unit cell structure factor*, is over positions  $\vec{r}_j$  of atoms within the unit cell. By the convolution theorem, the crystal's scattering amplitude in reciprocal space is equal to the product of the lattice and unit cell structure factor. The coherent scattering signal is therefore a discrete sampling of the unit cell structure factor at individual Bragg peaks with momentum transfers corresponding to vectors of the reciprocal lattice.

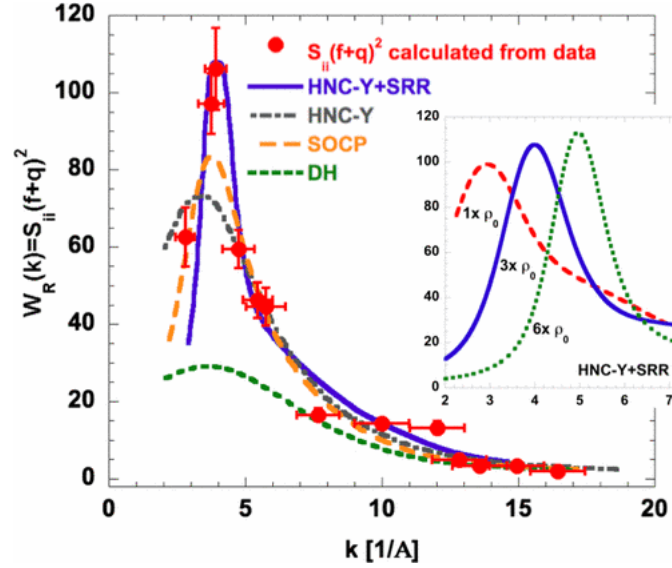
In the context of XRD from a material undergoing thermalization under fs XFEL heating, the crystal scattering amplitude's decomposition into lattice and unit cell components has a direct correspondence to interpretation of structural change. The onset of long-range lattice disorder is readily identifiable as a quenching in Bragg peaks roughly proportional to  $e^{-q^2}$ . Evolution of the unit cell structure factor, on the other hand, is dependent on the details of atomic level populations and the material's finite-temperature electronic structure, and can be used as a test of competing theoretical models of both.

(need cites and discussion of the existing literature on XRD of XFEL-heated WDM)

### 1.3.3 X-ray absorption

X-ray absorption spectroscopy (XAS) may be used to measure the structure and unoccupied electronic density of states of WDM systems. The information available by X-ray absorption near-edge spectroscopy (XANES) and X-ray absorption fine structure (XAFS) is the same

Figure 1.4: Experimental elastic scattering intensity of shock-compressed Al at OMEGA-60, compared to several hypernetted chain (HNC), Debye-Hueckel (DH), and screened one-component plasma (SOCP) models. (cite Ma et al.)

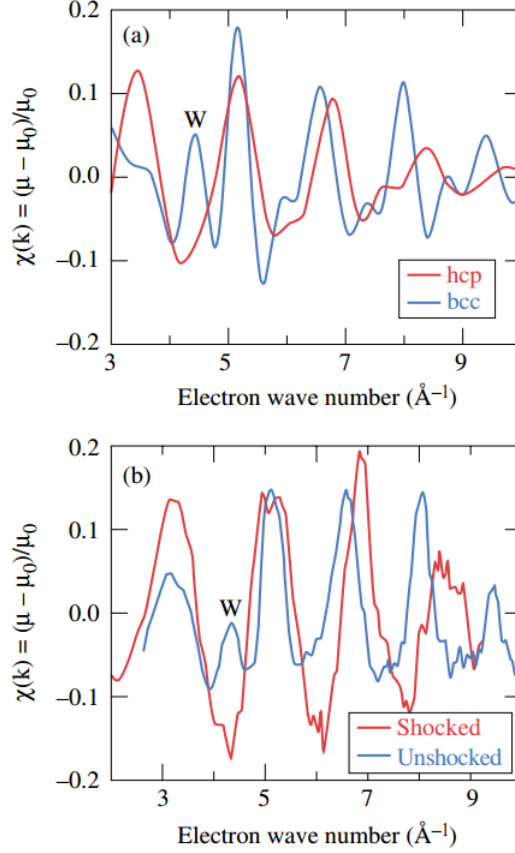


as in other scientific contexts, but the experimental implementation differs in a few respects. In all instances, the short duration of WDM states requires instantaneous collection of absorption spectra using a source with broad-band spectrum. At laser plasma facilities this is arranged using a spherical capsule of CH polymer imploded using a long-pulse laser (cite yaakobi 2003) that emits a thermal spectrum with a  $\sim 1$  MeV temperature (check this). This so-called broadband backlighter has been used to collect XAFS for the study of compression-induced phase transitions, such as that from bcc to hcp Fe driven by ns shock-compression (cite Yaakobi 2005).

XANES measurements on dense plasma have also been performed at laser plasma facilities. This requires narrower-band illumination compared with XAFS, which has been achieved using short pulse laser-driven multicomponent X-ray fluorescence backlighters. Levy et al., for example, have used this technique to demonstrate XANES-based thermometry based on measurement of the K-edge slope in Al isochorically heated to 3 eV. (cite Levy et



Figure 1.5: FEFF calculation of XAFS for hcp and bcc phases of Fe (a), compared to experimental data taken on ambient and shock-compressed Fe at the OMEGA laser (b). (cite Yaakobi)

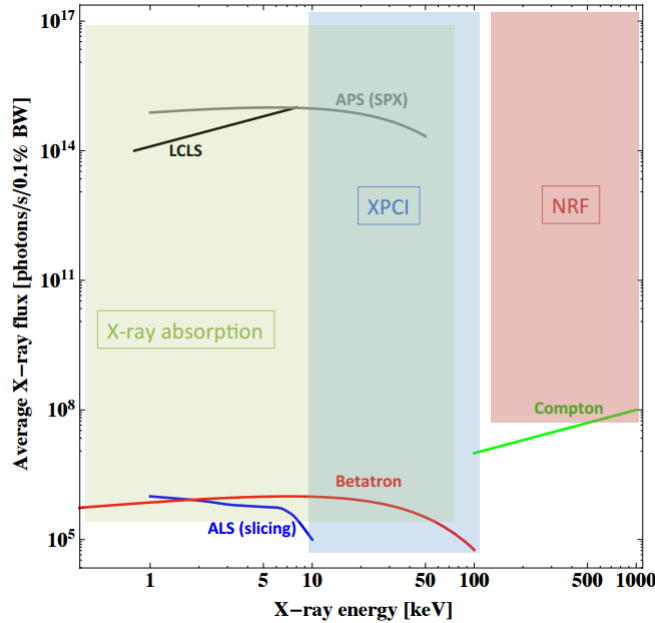


al).

Laser wakefield accelerator X-ray sources generate fs-duration broadband X-ray emission, affording time resolution that surpasses what is possible with laser-driven backlighters. This makes wakefield accelerators especially well-suited to X-ray absorption spectroscopy of WDM generated at XFEL facilities (cite Albert). The combination of wakefield accelerators with XFELs promises the unprecedented possibility of XFEL pump-probe experiments with simultaneous fs-duration interrogation of the target using broad- and narrow-band hard X-rays. This combination also enables XAS measurements of low-Z materials, which is much

more challenging at laser plasma facilities as a result of the mismatch between the short penetration lengths of x-rays near the K-edges of low-Z species and the relatively large target thicknesses (tens of microns) needed for effective laser ablation.

Figure 1.6: Parameter spaces of several x-ray techniques (X-ray phase contrast imaging (XPCI), x-ray absorption, and nuclear resonance fluorescence (NRF)), overlaid with curves indicating the regions of parameter space accessible by various x-ray source technologies and individual facilities (cite Albert).

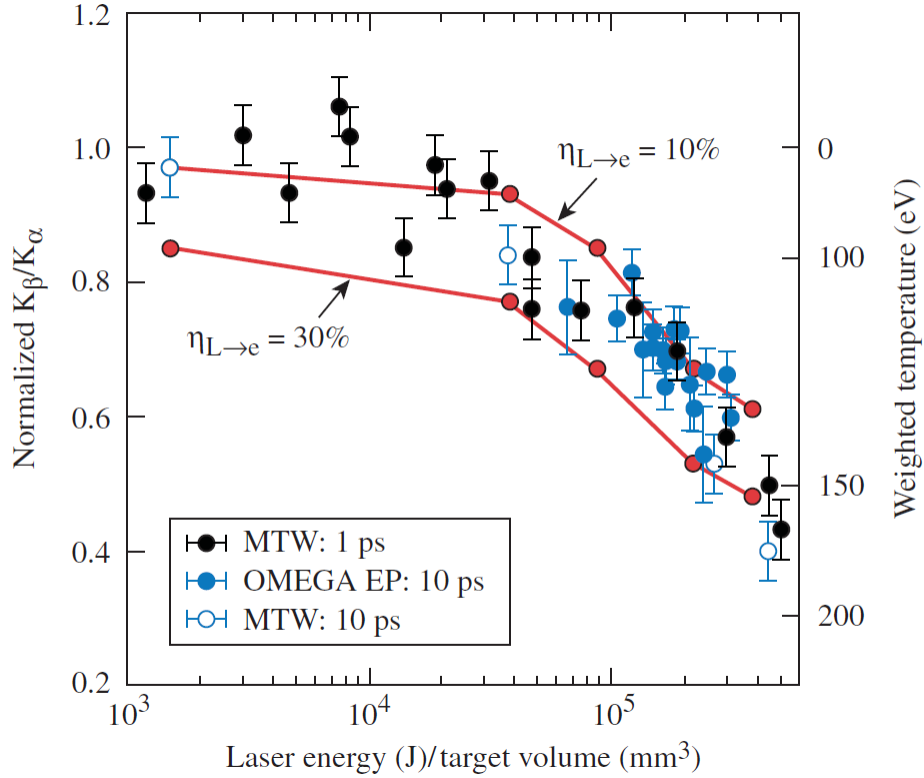


#### 1.3.4 X-ray Emission and X-ray Fluorescence

X-ray fluorescence spectroscopy (XRF) is an extensively used probe in experiments studying the interaction of high-intensity lasers with solid targets. In short-pulse laser experiments involving mid-Z elements heated to temperatures comparable to or larger than M-shell binding energies the ratio of  $K_\beta$  to  $K_\alpha$  emission is used as a measurement of temperature. Modeling the coupling efficiency between high-power laser and electrons in a solid-density target is of considerable significance to the effort to understand optical radiation-matter interactions

at high laser intensities ( $> 10^{19}$  W/cm<sup>2</sup>); in this context, inference of target heating using  $K_\beta/K_\alpha$  branching ratios provides a useful consistency check in the application of models to experimental data. (cite Myatt et al 2007, Nilson).

Figure 1.7: Experimental  $K_\alpha/K_\beta$  ratios of emission from Cu foil heated by short-pulse lasers, with inferred electron temperature on the right vertical axis. Model calculations are heating for hot electron coupling efficiencies  $\eta_e$  equal to 10% and 30% (cite Nilson)



X-ray emission spectroscopy (XES), the finer-grained cousin of XRF, provides more detailed information on the occupied density of states in a material and can be sensitive to valence-level excitations in the ‘tepid’ transitional regime between ambient and warm dense matter states (reference XES figure from the LD67, maybe get some cites). It has seen use primarily at XFEL facilities, where higher shot rates and probe intensities make the collection of datasets with satisfactory statistical quality easier. (cite photosystem 2 XES

papers). The advent of XFELs as the first high-intensity, monochromatic, and tunable WDM probes has also enabled resonant inelastic X-ray scattering (RIXS) measurements, which has made possible the direct measurement of ionization potential depression on a fs timescale, as demonstrated by Vinko et al. (cite Vinko, Ciricosta.).

#### **1.4 *Dissertation Outline***

The overarching theme in this thesis is the relationship, and frequent feedback, between scientific discovery and the development of new experimental technique. To begin, in chapter 2 I introduce a scheme for single-shot measurement of the static structure factors of disordered dense plasmas produced at large-scale laser facilities such as Omega and NIF. In Chapter 3 I present an experimental observation of nonlocal heat transport by keV-scale electrons in a nanophase material and consider the question of how this effect can be used to improve WDM experiments conducted at XFELs via optimized nanostructured target design. In chapter 4 I discuss experimental results of a recent experiment at the LCLS in which we established bounds on the timescales for thermalization of the lattice in XFEL-heated metal oxides and measured the consequences of XFEL heating on electronic charge density, with subsequent comparisons to different model predictions. In chapter 5 I describe an instrument-development effort toward a disposable CMOS-based X-ray camera for use in experimental environments hostile to electronics, particularly laser plasma facilities. Finally, in chapter 6 I introduce UW-XAP, a software tool for streamlined realtime data collection and analysis at the LCLS.

## Chapter 2

### PHYSICS OF PENELOPE

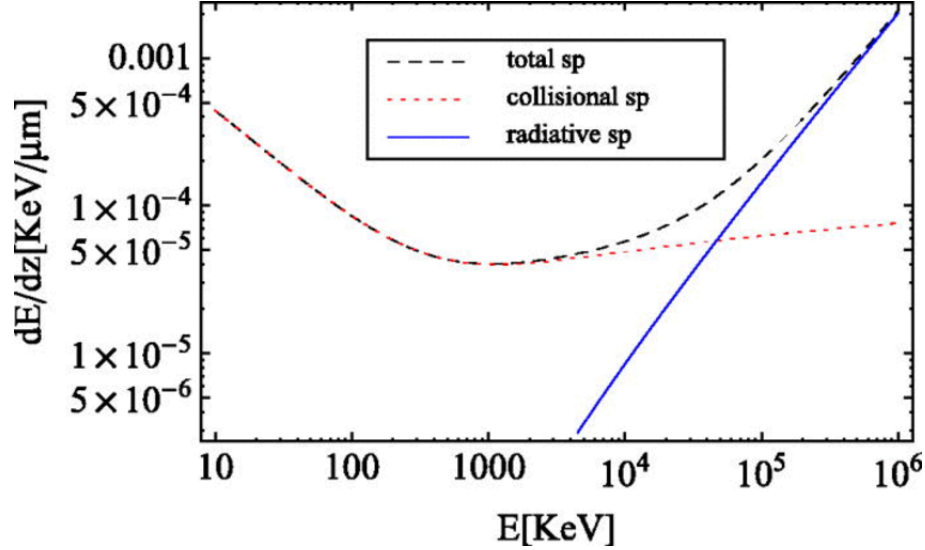
PENELOPE performs Monte Carlo simulations of coupled electron-photon transport in arbitrary materials in the energy range of 100 eV to 1 GeV. It uses a mixed simulation method that treats soft interactions (that is, those involving small angular deflections) with a multiple-scattering approach while individually simulating hard interactions. It is paired with a geometry-definition program, PENGEO, that allows defining samples with volumes of different material composition separated by arbitrary quartic surfaces.

#### **2.1 *Types of interactions***

In this section we consider the interactions that must be simulated to accurately model the spatial distribution of energy in a nanostructured target material heated by x-ray photons with energy on the order of 10 keV. PENELOPE simulates the following interactions: electron scattering (elastic and inelastic), Bremsstrahlung emission, photon scattering (both elastic (Rayleigh) and inelastic (Compton)), photoelectric absorption and Auger emission, x-ray fluorescence, and pair production and annihilation. Figs. 2.1 and ?? show the energy dependence of the relative strengths of the above electron and photon interactions, respectively. Several of the processes have negligible or nonexistent roles on the  $\leq 10$  keV energy scale considered in the current work, allowing us to limit our scope to the electron scattering and photoabsorption (with consequent fluorescence and Auger emission).

In what follows we introduce the physics of photoabsorption and elastic and inelastic scattering with attention to each process's contribution to the spatial distribution of deposited energy in a relaxation cascade beginning with photoionization by a hard x-ray photon. We discuss standard modeling approaches relevant to the 100 eV-10 keV regime, in addition

Figure 2.1: Collisional and radiative electron stopping powers as a function of energy (cite)

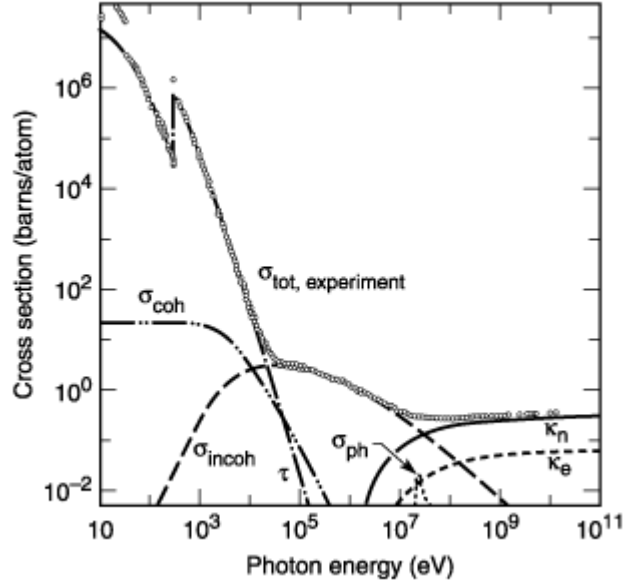


to cursory overviews of PENELOPE's treatments within the limited scope relevant to the current regime of interest.

### 2.1.1 Fluorescence

Fig (insert fig. 2.2 from penelope manual) illustrates the photoionization of inner atomic shells and introduces the notation used to describe atomic energy levels and transitions between them. Both the photoelectric effect and secondary (Auger) emission resulting from high-energy atomic excitations can be accurately modeled using established treatments that combine theoretical calculation of atomic states via self-consistent modeling (cite Pratt et al. 1973) with experimental data. Associated quantities are compiled in databases; PENELOPE uses tabulated ionization energies from Carlson (cite Carlson et al.) and photoelectric cross sections from the LLNL Evaluated Photon Data Library (EPDL). The EPDL additionally provides emission probabilities for fluorescence photons and Auger electrons in the relaxation of ionized atoms to the ground state.

Figure 2.2: Photon cross section components in C as a function of energy (cite LCL and Hubbell 1980)



### *Assumptions*

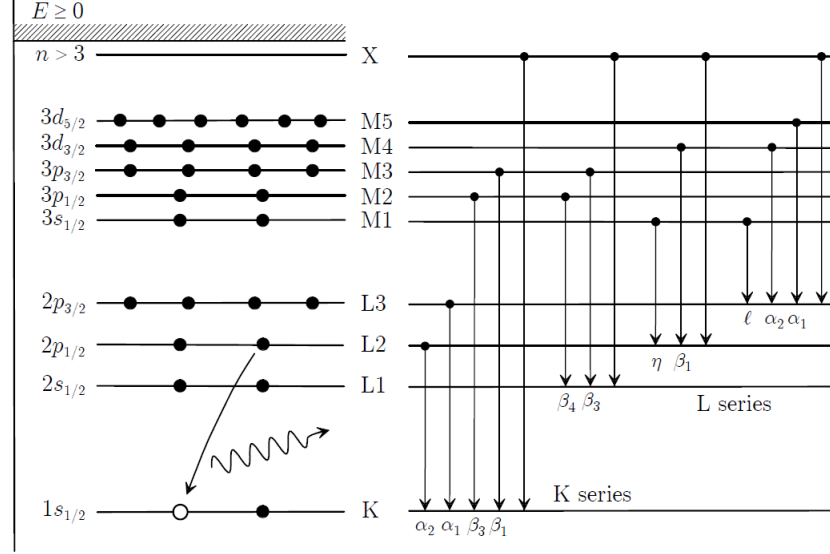
The above data sources are known to be accurate to the 1% level above 1 keV, under the condition (assumed by PENELOPE) of low incident photon densities, such that only single-electron transitions occur (cite PENELOPE manual).

PENELOPE assumes that incident photons are unpolarized and consequently fails to reproduce the polarization-dependent angular distribution (cite?) of emitted electrons. We note that it does incorporate the angular distribution from Sauter's (cite sauter 1931) treatment of relativistic photoelectron emission—which, however, reduces to isotropic emission in the nonrelativistic regime covered here.

#### *2.1.2 Elastic scattering*

Elastic scattering of electrons refers to interactions that do not alter target atoms' states.

Figure 2.3: Atomic energy levels of the first three principal quantum numbers (left) and corresponding allowed radiative transitions (right).



The simplest widely-used model for elastic scattering of electrons in a solid is the semi-classical approach of Wentzel and Lenz (Egerton page 114 ), known as the Lenz model, which uses the Yukawa potential for the interaction between a fast electron and a target atom:

$$V(r) = \alpha^2 \frac{e^{-r/r_0}}{r} \quad (2.1)$$

The first Born approximation gives the amplitude for a particle's scattering off of a spherically symmetric potential as

$$f(\theta) \simeq -2 \frac{m}{\hbar^2 q} \int_0^\infty r V(r) \sin(qr) dr \quad (2.2)$$

Substituting (how do I reference equations) into (2.2), yields

$$f(\theta) \simeq -2 \frac{m \alpha^2}{\hbar^2 q} \int_0^\infty e^{-r/r_0} \sin(qr) dr = -\frac{2m \alpha^2}{\hbar^2 (r_0^{-2} + q^2)}, \quad (2.3)$$

therefore giving the following differential scattering cross section:

$$\frac{d\sigma}{d\Omega} = |f(\theta)|^2 = \frac{4Z^2}{a_0^2 k_0^4} \frac{1}{(\theta^2 + \theta_0^2)^2},$$



where  $k_0 = m_0 v$  is the momentum of the incident electron,  $\theta_0 = (k_0 r_0)^{-1}$  is the characteristic angle for elastic scattering and  $a_0 = 4\pi\epsilon_0\hbar^2/m_0e^2$  is the Bohr radius.

Using the Thomas-Fermi model, Wentzel and Lenz obtain  $r_0 = a_0 Z^{-1/3}$  (cites). Doing this substitution and integrating over scattering angles gives

$$\sigma_e = \int_0^\pi \frac{d\sigma}{d\Omega} 2\pi \sin\theta d\theta = \frac{4\pi}{k_0^2} Z^{4/3} \quad (2.4)$$

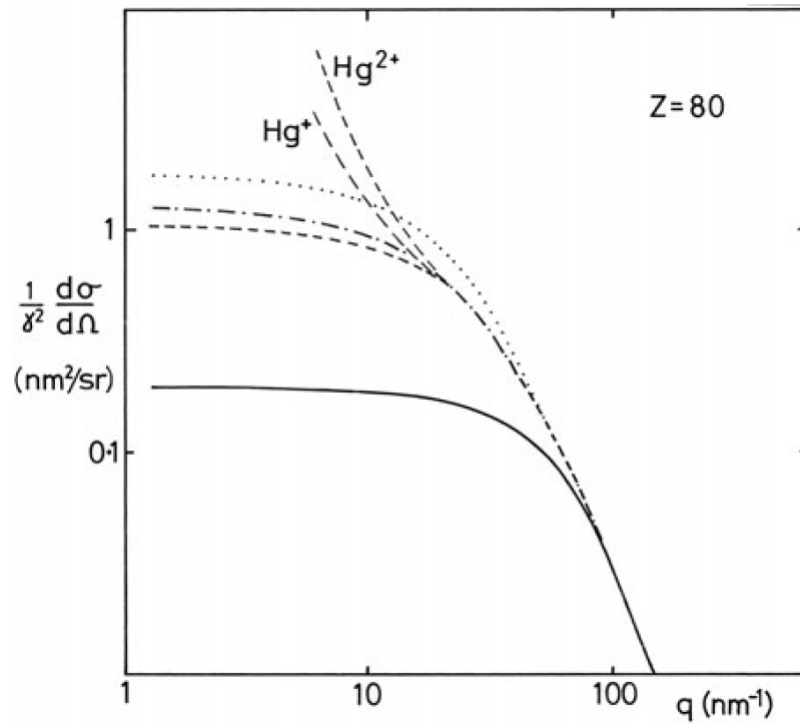
We thus see that the angular deflections produced by elastic scattering decrease with increasing energy. For 10 keV electrons  $\theta_0 \simeq 0.1$  rad and  $\sigma_e = 4.2 \times 10^{-20}$  m<sup>2</sup>. The elastic mean free path, an alternate measure of the collision frequency, is equal to  $\lambda_e = 1/(\sigma_e n)$ , where  $n$  is atomic number density. As an example, inserting the value of  $n$  for Fe yields 2.8 Å (at the same 10 keV electron energy) (*sounds far too small; check this calculation*). This corresponds to a large number of collisions on length scales of interest ( $\lesssim 10$  nm) which, combined with the appreciable value of the characteristic scattering angle, demonstrates that elastic scattering has a substantial influence on the propagation of electrons below 10 keV.

Taking the atomic number of density of Fe, the mean free path between inelastic collisions is (insert the right expression) = (insert the right number). The corresponding expectation value of angular deflection per distance traveled is (insert the right number). In comparison, the inelastic mean free path of 10 keV photons in Fe (potential see-saw here is (insert number). where should i introduce inelastic scattering?) This suggests that path deflections caused by elastic scattering will have a significant influence on the spatial distribution of energy deposited 10 keV-scale electrons in Fe and other mid-Z materials.

Despite its simplicity, the Lenz model gives total cross sections to within 10 % for light elements (cite Geiger 1964). For heavier species it underestimates the small-angle differential cross section (Fig. 2.4) but correctly reproduces the large-angle DCS.

More accurate approaches use iterative (e.g. Hartree-Fock) solutions to the Schroedinger equation (or of the Dirac equation, where relativistic and spin effects are needed) to solve for the atomic potential. (cite rez 1984 or starostin, applicability of the born approximation to collisions between electrons and excited atoms). Additionally, partial wave approaches can

Figure 2.4: Angular dependence of elastic DCS of 30 keV electrons from a Hg atom under the Lenz model using the Wentzel potential (solid), and based on Hartree-Fock (dotted), Hartree-Slater (dot-dashed) and Dirac-Slater (dashed) wavefunctions. (**Reference1** )



be used to avoid the Born approximation in regimes for which it fails (low electron energy and high-Z species). PENELOPE combines the above techniques: it solves the partial-wave expanded Dirac equation with a potential based on the Dirac-Fock electron density of Desclaux (1975, see citation on pg 102 of penelope manual) and exchange interaction of Furness and McCarthy (1973). We will elaborate on PENELOPE's modeling of elastic scattering only within the narrow concern of assessing its range of applicability; for more detail the reader may refer to chapter 3 of the PENELOPE manual.

## 2.2 Inelastic scattering

Inelastic collisions are the dominant mechanism for energy loss of electrons up to above 10 keV (2.1).

In an atomic system, the differential cross section for a transition from initial state wavefunction  $\psi_0$  to final state wavefunction  $\psi_n$  is

$$\frac{d\sigma_n}{d\Omega} = \frac{m_0^2 k_1}{2\pi\hbar^2 k_0} \left| \int V(r) \psi_0 \psi_n \exp(iqr) d\tau \right|^2 \quad (2.5)$$

where  $\mathbf{k}_0$  and  $\mathbf{k}_1$  are the wave vectors of the incident electron before and after scattering and  $q = \hbar(\mathbf{k}_1 - \mathbf{k}_0)$  is the corresponding momentum transfer.

At nonrelativistic velocities the potential between electron and atom may be expressed as the following sum of Coulomb potentials of the nucleus and atomic electrons:

$$V(r) = \frac{Ze^2}{4\pi\epsilon_0 r} - \frac{1}{4\pi\epsilon_0} \sum_{j=1}^Z \frac{e^2}{|\mathbf{r} - \mathbf{r}_j|} \quad (2.6)$$

Substituting the second term of equation 2.6 into 2.5, we note that the nuclear potential is independent of the coordinates of the atomic electrons and can therefore be removed from the integral. The orthogonality of the wave functions  $\psi_n$  implies that the nuclear potential does not contribute to inelastic scattering; the expression for the differential cross section of inelastic scattering is therefore:

$$\frac{d\sigma_n}{d\Omega} = \left( \frac{4}{a_0^2 q^4} \right) \frac{k_1}{k_0} \left| \epsilon(q) \right|^2, \quad (2.7)$$

where

$$\epsilon_n = \int \psi_n \sum_j e^{iqr_j} \psi_0 d\tau. \quad (2.8)$$

The generalized oscillator strength is an important related quantity:

$$f_n(q) = \frac{E_n}{R} \frac{\left| \epsilon_n(q) \right|^2}{(qa_0)^2}, \quad (2.9)$$

where  $R = (m_0 e^4 / 2)(4\pi\epsilon_0 \hbar)^{-2}$ , the Rydberg energy, and  $E_n$  is the energy change of the transition.

The GOS is in general continuous and therefore better expressed as a density with dimensions 1/energy, i.e.  $df(q, E)/dE$ . This allows us to write the double-differential cross section of inelastic scattering:

$$\frac{d^2\sigma}{d\Omega dE} = 4REq^2 \frac{k_1}{k_0} \frac{df}{dE}(q, E), \quad (2.10)$$

TODO: calculate a typical inelastic scattering cross section for comparison elastic scattering. The fact that the ratio is of order unity demonstrates that both matter.

### 2.2.1 Dielectric function

While this formulation makes it possible to calculate the GOS and associated quantities starting from an atomic model, in solid state systems the scattering cross section of outer-shell bonding is influenced by collective effects and chemical bonding. It's therefore preferable to describe the inelastic scattering of an electron off a solid using the solid's dielectric response function,  $\epsilon(q, E)$ .

Ritchie (cite Ritche 1957) showed, using Poisson's equation and fourier transforms, that an electron moving in the z-direction in an infinite medium experiences a force of the following magnitude opposite its direction of motion:

$$\frac{dE}{dz} = \frac{2\hbar^2}{\pi a_0 m_0 v^2} \int \int \frac{q_y \omega \text{Im}[-1/\epsilon(q, \omega)]}{q_y^2 + (\omega/v)^2}, \quad (2.11)$$

where  $q_y$  is the component of the momentum transfer vector perpendicular to  $v$  and  $\omega = E/\hbar$  is an angular frequency. This quantity is referred to as the stopping power. It can be expressed in terms of the previously-defined DDSCS:

$$\frac{dE}{dz} = \int \int nE \frac{d^2\sigma}{d\Omega dE} d\Omega dE, \quad (2.12)$$

where  $E$  is energy loss and  $\Omega$  is solid angle. By equating equations 2.11 and 2.12 in the small-angle limit it can be shown, by comparison with the atomic treatment (cite), that

$$\frac{df}{dE}(q, E) = \frac{2E}{\pi E_a^2} \text{Im}\left[\frac{-1}{\epsilon(q, E)}\right],$$

thus demonstrating the equivalence of the atomic and dielectric approaches.

Note, finally, that the GOS fully determines the value of equation 2.10 within the first Born approximation. As such, given the potential of equation 2.5 all modeling of the inelastic scattering of electrons at intermediate energies (1 keV - 300 keV) reduces to construction of a GOS model.

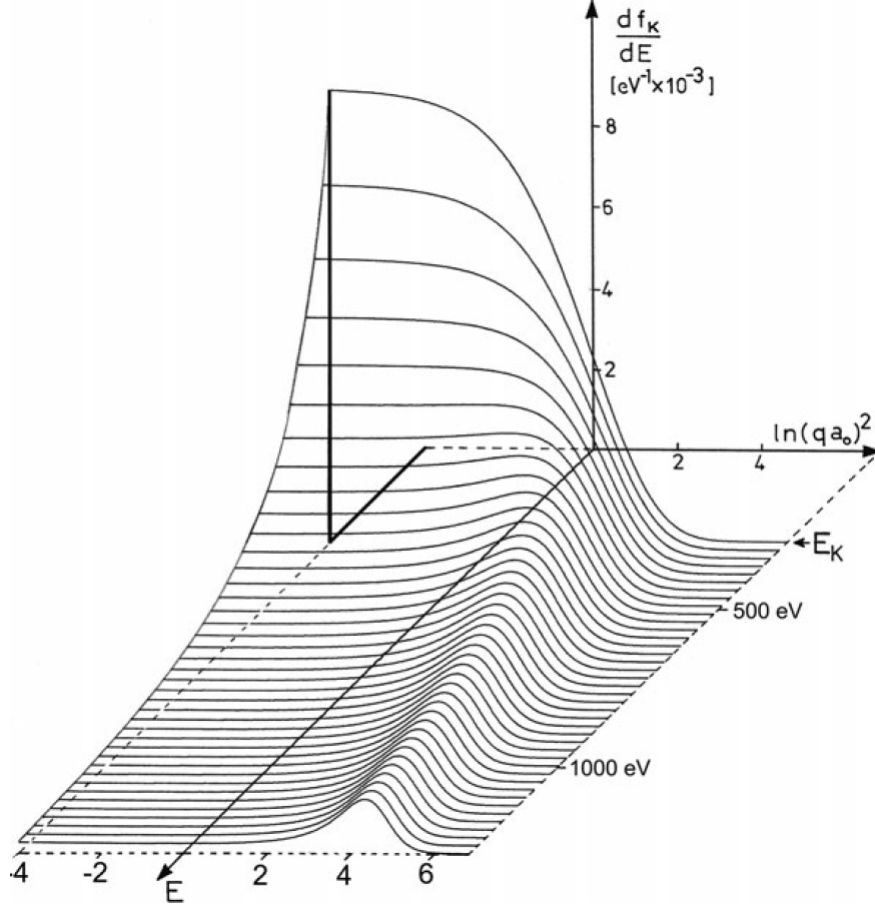
### *2.2.2 Modeling the generalized oscillator strength*

Analytical expressions for the GOS are known for only two simple cases of the free electron gas and hydrogen atom. In practice, however, it has been shown that the physics of inelastic scattering is mostly determined by a few global features of the GOS (cite Salvat and Fernandez-Varea, 1992) and that relatively simple models are therefore adequate in most situations.

The GOS is conventionally represented as a two-dimensional surface plot called the Bethe surface (Fig. 2.5). We identify two constraints on the behavior of the Bethe surface which any GOS model must reproduce. First, in the limit  $Q \rightarrow 0$ , the GOS of the dielectric formulation becomes proportional to the optical oscillator strength  $\text{Im}[-1/\epsilon(0, E)]$ , which is experimentally constrained by x-ray emission measurements. Second, in the limit of large momentum transfer the most probable energy loss is equal to the kinematically-determined value for collision between two free electrons,  $E = q^2/2$ . (cite Sorini). The corresponding trace in energy and momentum is a feature of the Bethe surface known as the Bethe ridge.

As in Compton scattering, the shape of cuts through the Bethe surface (i.e. spectra of scattered intensity as a function of energy at fixed momentum transfer) is determined by the momentum distribution of atomic electrons. Certain models, such as that of Sorini et al

Figure 2.5: Bethe surface for ionization of the K shell in C..... (cite)



(cite sorini 2006), derive a value for the width of the Bethe ridge from Fermi velocity calculations. PENELOPE adopts a simpler form based on the ‘ $\delta$ -oscillator’ model of Liljequist (cite Liljequist 1983) which splits the GOS into contributions from generalized ‘shells’ (each corresponding to either an atomic shell or a collective excitation). The total GOS under this model is a sum over indices  $k$  of the shells:

$$\frac{df(q, E)}{dE} = \sum f_k [\delta(E - E_k) \Theta(q_k - q) + \delta(E - q) \Theta(q - q_k)],$$

where for the  $k$ th shell  $f_k$  is the shell’s number of electrons,  $q_k$  is the cutoff recoil energy, and  $E_k$  is the shell’s resonance energy.  $Q_k$  is equal to the shell’s binding energy  $U_k$  (excluding

the band, for which it is set to 0), and  $E_k$  is computed from  $U_k$  and the material's mean electron density, following Sternheimer (cite Sternheimer 1952). Within this model the GOS is fully determined by the shells' occupations and cutoff (binding) energies  $U_k$ , which PENELOPE obtains from Carlson (cite Carlson 1975). It is possible, optionally, to direct PENELOPE to fit its GOS model to experimental stopping power data provided in material input files. It performs this fit through reweighting of the GOS model's oscillators (*this is actually a guess, as the PENELOPE manual is totally opaque about how the GOS/DDCS is fit to stopping power input data. Better understanding would require me to revisit PENELOPE's code or contact the authors*).

Substantial additional detail on the construction and interpretation of PENELOPE's GOS model can be found in its manual.

### **2.3 Accuracy and useful regimes**

In the context of simulation of nanostructured materials, errors in PENELOPE's DCSs for electron scattering originate from both (1) the limited range of validity of PENELOPE's physical models with respect to the bulk properties PENELOPE seeks to reproduce, and (2) from the difference between scattering DCSs of ambient-condition bulk materials on the one hand and high-temperature nanostructured materials on the other. We address these two issues in combination.

As mentioned previously, a material's inelastic scattering DCS is fully determined by its loss function, the imaginary component of the dielectric function. Any difference between the responses of bulk and nanophases arises from the contribution to the loss function of collective electronic excitations, i.e. plasmons. Plasmon modes in nanostructured materials form a large research topic on their own (find and cite review article on surface plasmons in nano-materials), but there has been little (no?) (cites) prior work in the context of high-temperature dense matter. The study of heated nanophase materials thus manifests itself as both a problem and an opportunity. On the one hand, the lack of experimental data and accurate modeling makes it impossible to fully quantify the inaccuracy of simula-

tions of ambient, bulk materials. On the other hand, XFEL heating experiments could be used to discriminate between computed dielectric response functions and their underlying finite-temperature electronic structure theory—to the extent that alternative models generate experimentally measureable differences in inelastic DDCSs. We thus suggest that XFEL heating of nanostructured materials could enable a joint modeling/experimental program to validate WDM electronic structure theory.

### 2.3.1 Low-energy loss DCS

In the current situation, wherein the plasmon contribution to the loss function is not known, we can take advantage of the fact that plasmon resonance are confined to energy losses smaller than approximately 100 eV. The influence of the low-energy region of the loss function on the spatial distribution of deposited energy can therefore be bounded using the continuous slowing down approximation (CSDA) of 100 eV electrons. The CSDA for electrons of energy  $E_0$  is the following integral over stopping power:

$$l_{CSDA} = \int_{E_{final}}^{E_0} \left(\frac{dE}{dz}\right)^{-1},$$

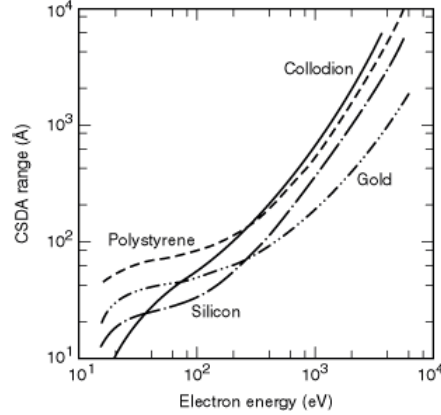
where  $E_{final}$ , the final energy of the electron, is usually taken to be 10 eV. For elements heavier than boron,  $l_{CSDA} < 10$  nm for  $E = 100$  eV. We therefore conclude that inaccuracy in treatments of collective excitations affect the spatial distribution of energy deposited by electrons on a length scale below 10 nm (Fig. 2.6)

### 2.3.2 Energy cutoffs

PENELOPE stops simulation of an electron's motion once its energy drops below a prescribed cutoff value; at the endpoint of an electron's simulated track all of the electron's final energy is deposited at its final position. The resulting distortion in the spatial distribution of deposited energy can be bounded, as above, using the CSDA. PENELOPE's cutoff energy can be set as low as 50 eV. Assuming this value is chosen, the resulting error is much smaller



Figure 2.6: CSDA range as a function of energy for several materials, based on stopping powers of..... (cite)



than the bound from section 2.3.1 on the error attributed to inaccuracy in the low-energy dielectric function. Simulation error due to PENELOPE's energy cutoff can therefore be safely neglected.

### 2.3.3 Elastic scattering

PENELOPE's use of the static field approximation in its elastic scattering model introduces a low-energy error in the DCS due to the effect of the polarizability of atomic charge (cite Salvat 2003). The size of this error is 20% at 1 keV and 50% at 100 eV (PENELOPE manual, pg. 102). The CSDA range at 1 keV, where uncertainty at the DCS level is considerable, ranges from 10 nm for high-Z elements to over 100 nm for low-Z ones. Because the results of the PENELOPE simulations discussed in chapter (which chapter?) are sensitive to errors on the 10 nm - 100 nm length scale, the CSDA does not usefully constrain the elastic DCS model's contribution to uncertainty in the spatial distribution of deposited energy.

A crude estimate taking into account the magnitude of uncertainty in the elastic DCS may be obtained by considering elastic scattering of an electron as a correlated random walk. Given a mean free path  $\lambda_e$  and characteristic scattering angle  $\theta_0$ , the number of steps after which the electron's direction of motion becomes uncorrelated with its initial direction is of

the order  $n = \pi/\theta_0\lambda_e$ . The number of elastic scattering events an electron experiences as it slows from an energy of 1 keV to 100 eV (the previously-established—but arbitrary—cutoff below which the treatment of section 2.3.1 applies) is

sketch: basically I have to calculate the number of scattering events, and associated dephasing of the electron’s direction, for several ‘bins’ of energy between 100 eV and 1 keV. For each bin we calculate the equivalent number of steps under an uncorrelated random walk. This yields an expected displacement proportional to the square root of the number of steps in the uncorrelated random walk, which we can multiply by the elastic DCS uncertainty in order to get an associated displacement uncertainty. All displacement uncertainties can then be added in quadrature, yielding a final uncertainty.

## 2.4 *Inelastic scattering*

Inelastic scattering has much smaller characteristic angles than elastic scattering scattering but comparable total cross sections. As a result the influence of angular deflections by inelastic scattering on the propagation of electrons is relatively small. The effect of uncertainties in the inelastic scattering DDCS can thus be neglected, and we confine our attention to uncertainty at the level of the stopping power, a more coarse-grained quantity.

Fig 2.7 compares PENELOPE’s computed stopping powers and inelastic mean free paths (for what???) to several experimental datasets. The level of disagreement between different datasets is of the order 2 in the 1 keV - 10 keV energy loss range; the discrepancy between PENELOPE’s modeled stopping power and the experimental datasets is also of this order. Because all transport lengths are proportional to stopping power we must thus contend with a factor of 2 uncertainty in the length scale of computed spatial distributions—far larger than any of the other uncertainties we have considered until now.

The conclusions of chapter (WHICH CHAPTER?) can nevertheless be conserved, with one modification, if we consider PENELOPE’s error in modeling the 1 - 10 keV stopping power as an unknown constant-factor scaling in stopping power. Such an uncertainty corresponds to an unknown scaling of both (1) the length scale of spatial distributions of deposited

energy and (2) the flux magnitude of nonlocally-transported energy crossing a given material interface. To give a simple illustration, consider a one-dimensional configuration consisting of an infinite extent of source material from  $x = -\infty$  to  $x = \infty$ . When the sample receives x ray illumination of magnitude unity at position  $x_0$  the density distribution  $\rho(x)$  of deposited energy is given by a response function  $f(x)$  (fully determined by the sample material's stopping power and incident x-ray spectrum):  $\rho(x) = f(x - x_0)$ . If the material is uniformly illuminated by x rays in the region spanning  $x = 0$  to  $x = \infty$  then (in arbitrary units):

$$\rho(x) = \int_0^\infty f(x - x') dx'.$$

Under the substitution  $f(x) \rightarrow g(x) = f(cx)$  (equivalent to scaling  $dE/dz \rightarrow (1/c)dE/dz$  of the stopping power), and maintaining normalization of the response function, the distribution becomes:

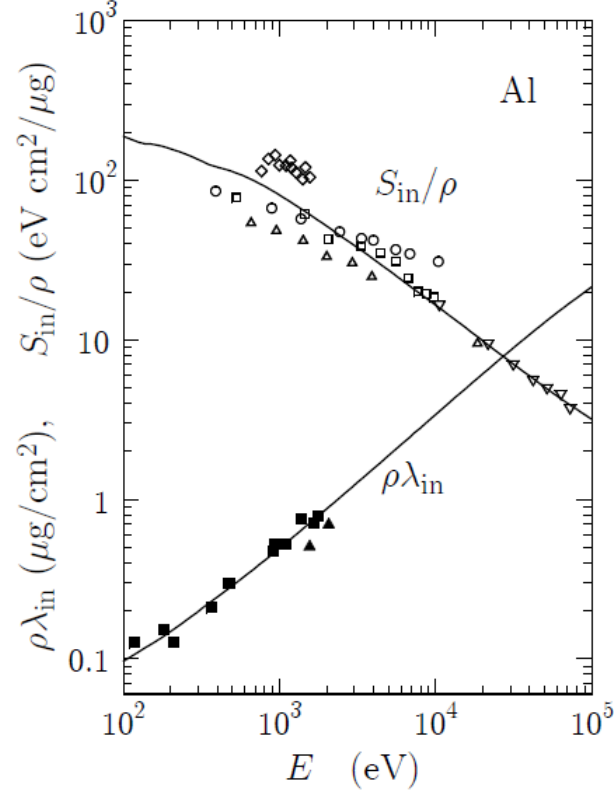
$$\rho'(x) = \int_0^\infty cf((c(x - x'))))dx = \int_{cx}^\infty f((u))u.$$

Therefore constant-factor scaling of the stopping power is equivalent to a change in units of length, implying that, under our assumed form of the uncertainty in  $dE/dz$ , and adding the assumption that the unknown scaling factor  $c$  is equal for all materials, the simulated spatial distributions of deposited energy density are correct up to a uniform scaling of the sample geometry.

## 2.5 Dosimetry

PENELOPE's dosimetry includes both linear energy transfer from radiation to matter and the contribution of particle track ends, as mentioned in section 2.3.2. At the energy scales of interest the former contribution may be neglected, and the distribution of energy deposited by a particle shower is entirely dependent on simulated inelastic scattering events. PENELOPE's dosimetry calculation is tied to the termination of electron tracks: when an electron's energy drops below the (previously-defined) cutoff value its simulation ceases, and

Figure 2.7: Stopping power and inelastic mean free path for electrons as a function of energy in Al..... (cite)



its entire energy is deposited at the track's endpoint. Similarly, the energy loss of soft inelastic collisions (ones having energy loss greater than the cutoff energy  $W_{cc}$ ) is deposited locally (whereas hard inelastic collisions generate secondary electrons that are individually tracked).

Coarse-graining of the dose distribution is done by dividing the simulation volume into a three-dimensional grid of cells, in each of which PENELOPE calculates the total dose of deposited energy. This grid is defined by the parameters GRIDX, GRIDY, GRIZ and GRIDBN in PENELOPE's input.

## Chapter 3

# X-RAY FREE ELECTRON LASER-BASED STUDIES OF WDM

### 3.1 *X-ray Free Electron Lasers*

XFELs produce radiation of unprecedented brilliance (10 orders of magnitude higher than undulator radiation from third-generation synchrotron sources), full transverse coherence, pulse durations as short as 10 fs. This combination of capability far exceeds that possible with third-generation light sources and opens new frontiers in imaging and the interrogation of ultrafast processes in materials science and biology (cites). In this section we give an overview of the technology and its range of applications in the study of HED states of matter.

#### 3.1.1 *Physics of XFELs*

To describe the FEL interaction, we first consider the generic case of radiation emission from undulators, the type of insertion device used in both XFELs and the highest-brilliance beamlines at third-generation synchrotron light sources.

A simple time-of-flight argument may be used to obtain an intuitive understanding of radiation by a single electron in an undulator. A radiation wavefront co-propagating with an electron undergoing forced transverse undulation with a (longitudinal) period  $\lambda_u$  will move ahead of the electron. Constructive interference of the radiation field produced by successive undulations of the electron will occur at discrete values of the electromagnetic wavelength,  $\lambda_n$ , satisfying  $\lambda_n = \lambda_1/n$ , where  $\lambda_1$  is defined as the fundamental resonant wavelength. The time  $t$  taken for an electron to propagate one undulator period  $\lambda_u$  at speed  $v_z$  ( $t = \lambda_u/v_z$ ) is equal to that needed for a resonant wavefront travel the distance  $\lambda_u + n\lambda_n$ . Equating the propagation times for the wavefront and electron yields the relation (cite McNeil et al.)

$$\lambda_n = \frac{\lambda_u}{n} \left( \frac{1 - v_z/c}{v_z/c} \right). \quad (3.1)$$

More detailed treatment shows that, in the case of a helical undulator, only the fundamental mode has strong on-axis emission. (cites)

This describes the narrow spectral width of undulator radiation and the coherent addition of radiated wave amplitudes by a single electron over the length of an undulator. This constructive interference accounts for the much higher brilliance of radiation produced by an undulator, compared to a wiggler or bending magnet.

At a synchrotron light source electrons in a bunch have uncorrelated positions, and the undulator spectrum is therefore a simple incoherent sum of the emission of all individual electrons passing through it. An XFEL improves on this by creating a positional ordering electrons into ‘micro-bunches’ separated from one another by the radiation field wavelength. The coherent emission from multiple micro-bunches with  $N_b$  electrons each would be equivalent, in an idealized case where the micro-bunch dimension were much smaller than the x-ray wavelength, to that from point-like charges of magnitude  $eN_b$ , with a resulting factor of  $N_b^2$  enhancement in brilliance relative to that from an incoherently-emitting electron bunch. (cite)

Electrons in an undulator experience a longitudinal force from the radiation field that is modulated by its period. The consequent bunching of electrons with a period equal to the X-ray wavelength is a self-reinforcing process referred to as self amplified stimulated emission (SASE) (cites). Crucially, the occurrence of SASE requires a sufficiently strong initial radiation field, which third-generation synchrotron storage rings—having 100 ps-duration electron bunches—are not capable of producing. The key feature of an XFEL is its use of a linear accelerator to produce very compact electron bunches with sufficient electron density to bootstrap SASE.

### 3.1.2 XFELs and WDM generation

Maximum single-shot flux densities available at XFELs exceed  $10^4 \text{ J/cm}^2$ , sufficient to produce HED states with per atom energy deposition over 100 eV with uniform, volumetric heating. (TODO: how about better-focusing optics?). Because XFEL radiation is monochromatic it can be used as a probe for nearly all X-ray diagnostics useful for determination of the state variables of WDM, with the notable exception of XAS. Taken together, these characteristics make XFELs ideal for both producing and probing short-timescale dynamics of HED matter. (cites)

One of the most significant recent advances in XFEL technology is the generation of two-color pairs of hard X-ray pulses. This is done by production of time-delayed twin electron bunches (achieved either by illuminating the source cathode with a train of two laser pulses, or using an emittance spoiler) (cite Marinelli et al., Lutman et al.) and the addition of magnetic chicanes that introduce a time-energy correlation in the electron beam before the bunches' entry into the undulator. At the LCLS, two color X-ray pulse energies up to the mJ level—approaching the values of single-pulse SASE—have been demonstrated. X-ray arrival time delays are variable between 30 and 125 fs, and maximum color separations of up to 1.9 % of the photon energy have been demonstrated (cite Lutman).

Operating an XFEL in two-color mode opens up significant possibilities for truly time-resolved probes of WDM. In single-pulse operation the time evolution of an XFEL-heated target can, to some extent, be studied by variation of pulse duration. However, such a study yields a signal that, for each XFEL configuration, is a convolution over all states the target transitioned as it heated throughout each pulse's duration. In contrast, two-color operation offers two advantages:

- Temporal resolution: by choosing pulse energies that straddle an absorption edge of a chemical filter (in the case of an XRD probe), or of the target itself (in the case of an XES probe), signal from the pump pulse can be rejected. Varying pump-probe delay thus allows measuring the sample's temporal response to the pump.

- Uniformity of probed state: By additionally reducing the intensity of the probe relative to the pump, one can ensure that the probe is only a weak perturbation to the heated state generated by the pump.

The possibility of clean time-resolved studies of XFEL-generated WDM is quite attractive, given that the electronic relaxation cascade in a heated solid consists of several partially-overlapping stages of uncertain durations: i.e. collisional ionization by hot electrons; stimulation of long-wavelength collective excitations; and damping of large-q excitations through production of electron-hole pairs. Lack of prior information in the physics under scrutiny emphasizes the need for the highest-information diagnostics available.

## **3.2 HED physics at XFEL facilities**

### *3.2.1 Early experiments*

Initial efforts at FLASH and LCLS, the first free electron lasers operating at short wavelengths, have been focused on the creation of exotic states and the exploration of interactions of high-intensity hard X rays with matter. Thomas et al. and others have studied the Coulomb explosion of noble gas clusters, including the dynamics of nanoplasma formation (cite Thomas et al.). Using intense XFEL radiation Young et al. demonstrated the production of fully-stripped Ne atoms as well as induced X-ray transparency in ‘hollow’ atoms, a manifestation of ‘beating’ the Auger clock through ionization rates faster than the recombination times of core electrons. Their modeling of X-ray/atom interactions using a rate-equation based approach yielded predictions of atomic populations consistent with electron spectroscopy, providing an early validation of the application of population kinetics codes such as SCFLY to the simulation of XFEL-matter interactions. (cite Young, maybe cite SCFLY paper and check that it wasn’t originally written with XFEL simulation in mind).

Nagler et al. have similarly demonstrated saturable absorption of an L-shell transition in Al, where the long lifetime of 2p vacancies allowed complete depopulation within a single XFEL pulse at incident intensities on the order of  $10^{16}$  W/cm<sup>2</sup> and 92 eV photon energy.



(cite Nagler). This experiment was the first demonstration of a bulk, crystalline material in a high-energy density (and highly non-thermal) electronic configuration. (check that this is true).

### **3.3 Scientific Directions**

#### *3.3.1 Time dynamics of WDM states*

The ability of XFELs to produce such transient HED states invites basic questions about the creation of these states and their temporal evolution. Population kinetics codes such as SCFLY are a well-established tool to simulate the electronic evolution of an XFEL-heated material, but such codes are based on atomic physics treatments and cannot be all-encompassing, as they omit solid-state electronic structure as well as the interaction of electrons with the lattice of a solid-density system. Hau Riege et al. have examined electron-ion dynamics during heating by a single XFEL pulse, using comparison of Bragg diffraction from heated graphite with molecular dynamics simulation to quantify perturbation of the atomic lattice. They have identified melting of the graphite lattice within 40 fs pulses—far shorter in duration than the ps-timescale of electron-phonon coupling indicating an ultrafast phase transition. We revisit Hau-Riege’s conclusions in a different light in section (which section?), but their work pertinently demonstrates that the characterization of even coarse-grained quantities such as lattice thermalization timescales gives insight into the new physical regimes that XFELs are capable of producing and probing.

Similar observations apply to electron-electron thermalization in a solid, where damped collective excitations (ie. plasmons) may play a significant role as a bottleneck stage between absorption of XFEL photons and eventual thermalization of atomic electrons (cite Egerton, Sorini, maybe dig up cites from HEF paper).

As alluded to above, two-color XFEL operation is a promising potential means of addressing these questions.

### 3.3.2 Tests of Finite- $T$ electronic structure

The output quantity of a density functional theory (DFT) simulation is real-space charge density. At the same time, the real-space charge distribution of a crystalline XFEL target material can be interrogated via X-ray diffraction, which samples the unit cell structure factor at momentum transfers corresponding to vectors of the reciprocal lattice. Because a material's lattice typically does not have sufficient time to respond to the changing electronic configuration over the duration of an XFEL pulse, XRD from WDM states produced by an XFEL can be directly compared to predictions of frozen-lattice finite-temperature DFT calculations.

This observation has led Valenza et al. to generate predictions of the consequences of XFEL heating on the intensities of Bragg peaks in several materials using DFT calculations in VASP (cite Valenza et al.). They have shown that the information in the XRD signal is sufficient for discrimination between competing theoretical predictions, provided the XRD measurement is performed over a sufficiently wide range of momentum transfers. Valenza et al. demonstrate strong testable signatures of condensed-phase effects in each of LiF, graphite, diamond, and Be as a result of heating to temperatures on the order of 10 eV. A summary of their results is reproduced in Fig. ??.

The capability to test predictions of finite-temperature electronic structure models is a unique feature of XFEL-based experiments. We will explore the topic in some more detail in section (reference section), where we have the opportunity to apply it to experimental data.

## 3.4 Design of an XFEL heating experiment

One can identify several experimental desiderata shared by the majority of XFEL-based studies of WDM wherein the primary probe is X-ray diffraction:

- Maximization of information in the XRD signal
- Effective target heating so as to maximize the accessible range of energy densities

- Time resolution

Each of these can be achieved in one or more ways. Respectively:

- As alluded to in section (reference section), better-constrained estimates of real space charge density can be obtained by sampling a larger number of Bragg reflections. This requires probing a large momentum transfer range, made possible by using a high incident photon energy.
- In bulk samples, a high density of deposited energy requires matching the incident photon energy to a value at which the photoelectric absorption cross section is large. In section (reference section) we will introduce an alternate approach based on the design of structured targets that relaxes this constraint on incident photon energy.
- Wherever a single XFEL pulse is used to both heat and probe a sample, a limited degree of sensitivity to the time-evolution of transient states can be had by varying time duration. Two-color XFEL operation, however, is much more attractive. However, it suffers from tradeoffs: most notably experimental complexity and reduced signal, due to the need for attenuation of the probe pulse relative to the pump.

These goals, and the tradeoffs that accompany them, are important context for both the experimental work described in the next section and the modeling-based exploration of experimental technique discussed in section (reference section).

### **3.5 *Experimental Work***

In the following I describe several experimental results arising from two beam runs at the Matter of Extreme Conditions (MEC) endstation at the Linac Coherent Light Source (LCLS) in June of 2014 and January of 2016. The studies conducted addressed questions about the relative magnitudes, and time scales, of lattice and electronic heating in various solids, mainly

metal oxides. The primary diagnostic was XRD, with which we measured changes in electronic charge distribution as a function of incident flux, with the eventual goal of comparison to finite-T condensed matter electronic structure theory, as described in (reference section). The secondary diagnostic—used in a subset of the studies—was a von Hamos X-ray emission spectrometer with a highly annealed pyrolytic graphite (HAPG) analyzer crystal and 9 eV energy resolution, with which heating-induced line shifts and changes in valence-level emission were measured.

Throughout these measurements the XFEL beam was brought to a focus at the sample location using a stack of Be lenses. Flux incident on-sample was altered through a combination of beam attenuation and variation of the focal spot diameter between minimum and maximum values of 2 and 58 microns. XRD data was collected on a quad CSPAD solid state detector downstream from the sample (cite CSPAD paper).

In samples wherein the signal was weak compared to time variations in the area detector pedestal values, additional processing was performed in order to reconstruct signal incident on the detector. This is described in more detail in section (reference section), which details analysis and modeling of electronic heating based on an XRD dataset of XFEL-heated MgO.

### *3.5.1 Testing Lattice Thermalization in XFEL-heated Solid State Systems*

Fig. 3.4 (a, b) displays the progression of Bragg peak intensities as a function of incident flux for two different  $\text{Fe}_3\text{O}_4$  targets heated by 45 fs XFEL pulses. It demonstrates monotonic declines in the intensities of all Bragg peaks as a function of flux density, with the exception of the 222 peak, which rises to a maximum at the second-lowest flux density point before declining.

It is straightforward to evaluate the relative contributions of thermalization of electronic and lattice degrees of freedom to the XRD signal's evolution as a function of heating. The main distinguishing feature between these two components is that the latter causes Debye-Waller quenching of Bragg peak intensities that is approximately proportional to  $e^{-q^2\langle u^2 \rangle}$ , where  $q$  is momentum transfer and  $u$  is atomic displacement. Fig. 3.5 compares the experi-

mental data to this Debye-Waller progression for several different values of RMS atomic displacement. The experimental data shows a complete lack of Debye-Waller-like  $q$ -dependence in Bragg peak intensities at high levels of heating, signifying that the XRD response is strongly dominated by reorganization of electronic charge density within a unit cell.

The electronic response of  $\text{Fe}_3\text{O}_4$  to XFEL heating can be further interpreted through comparison of the data to a simple atomic form factor-based model of ionization (the model is described more specifically in section (reference section)). We find that the model reproduces the anomalous rise in intensity of the 222 reflection (reference figure) via a loss of destructive interference between the valence wavefunctions of O and Fe as both are simulataneously ionized. (cite paper in preparation).

Figure 3.1: Operation of an x-ray free electron laser (cite McNeil). Electrons enter the undulator with random phases and originally emit incoherent radiation at the undulator's resonant wavelength. As the electrons propagate, random fluctuations in the radiation field causes them to bunch at the resonant wavelength and emit coherently.

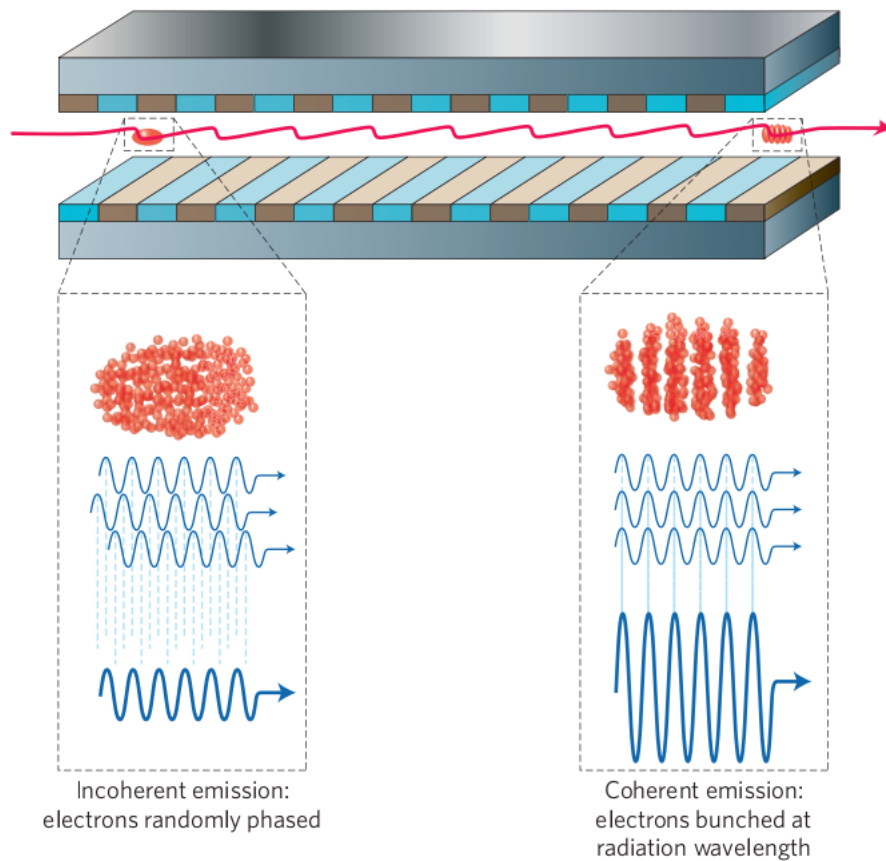


Figure 3.2: Schematic representation of a two-color XFEL x-ray diffraction measurement wherein a chemical filter is used to reject pump photons.

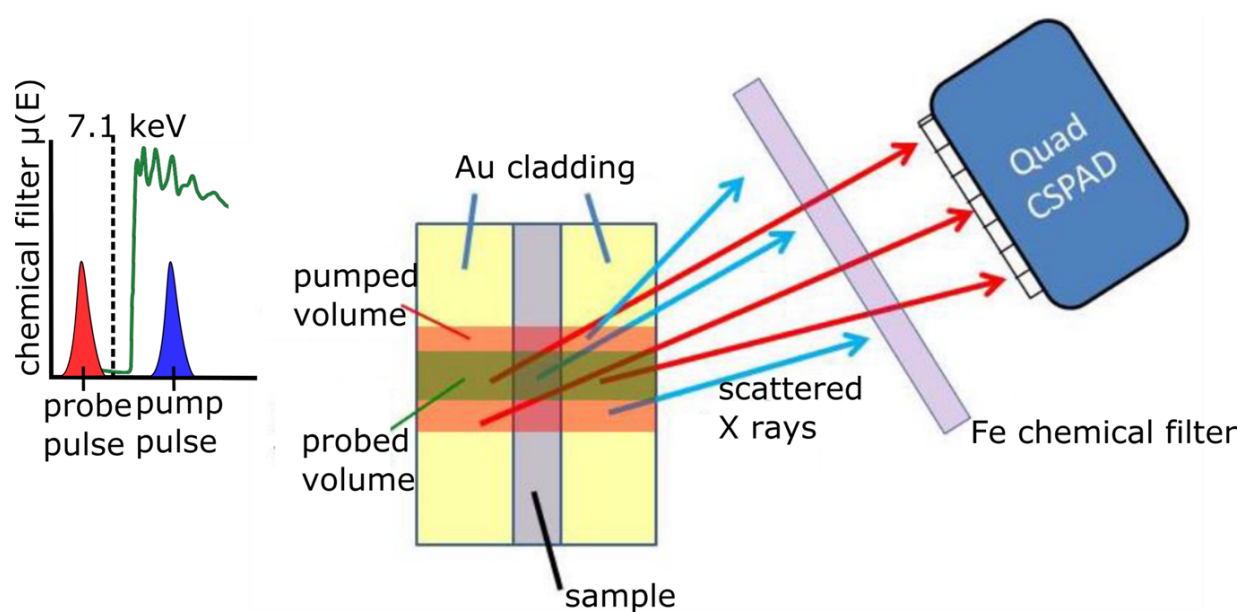


Figure 3.3: Left: intensity of diffraction peaks as a function of temperature, using finite-temperature DFT calculations in VASP; right: intensity of diffraction peaks as a function of ionization, using an atomic form factor-based model of ionization. The four simulated compounds are (from top to bottom) LiF, diamond, graphite, and Be. Taken from Valenza et al. (cite Valenza et al.)

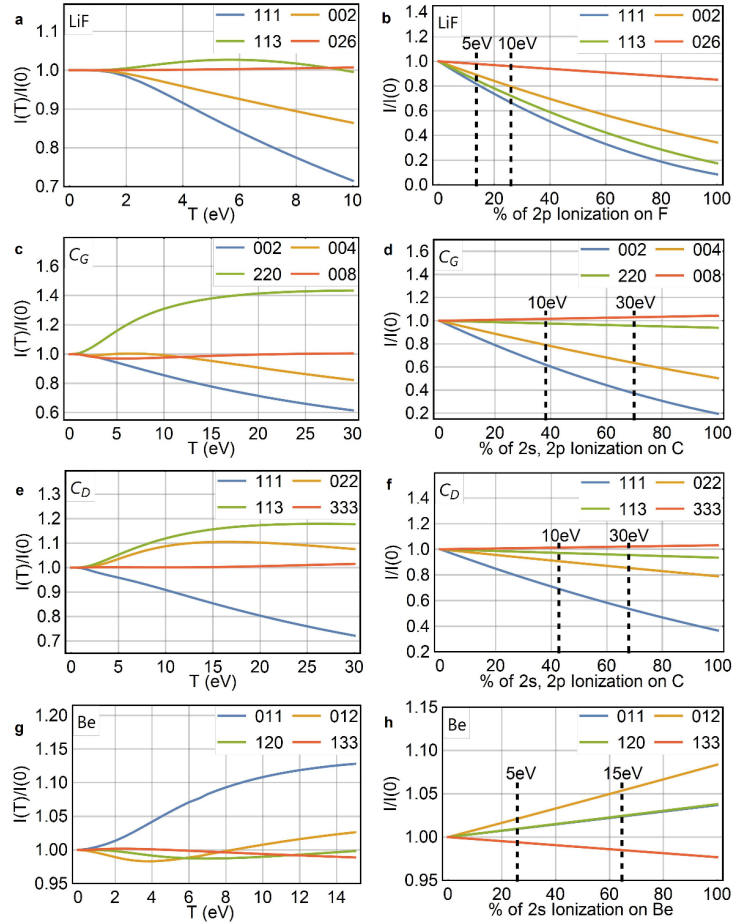




Figure 3.4: Progression of Bragg peak intensities as a function of incident x-ray flux density for (a) microphase and (b) nanophase  $\text{Fe}_3\text{O}_4$ , normalized to the intensity of the lowest-flux density point. (c) displays the progression of Bragg peak intensities as a function of electron ionization in an atomic form-factor based model wherein the Fe 3d and O2p electrons are first ionized, followed by the more tightly-bound Fe 4s and 3p, and O 2s electrons. (cite Fe3O4 paper in preparation)

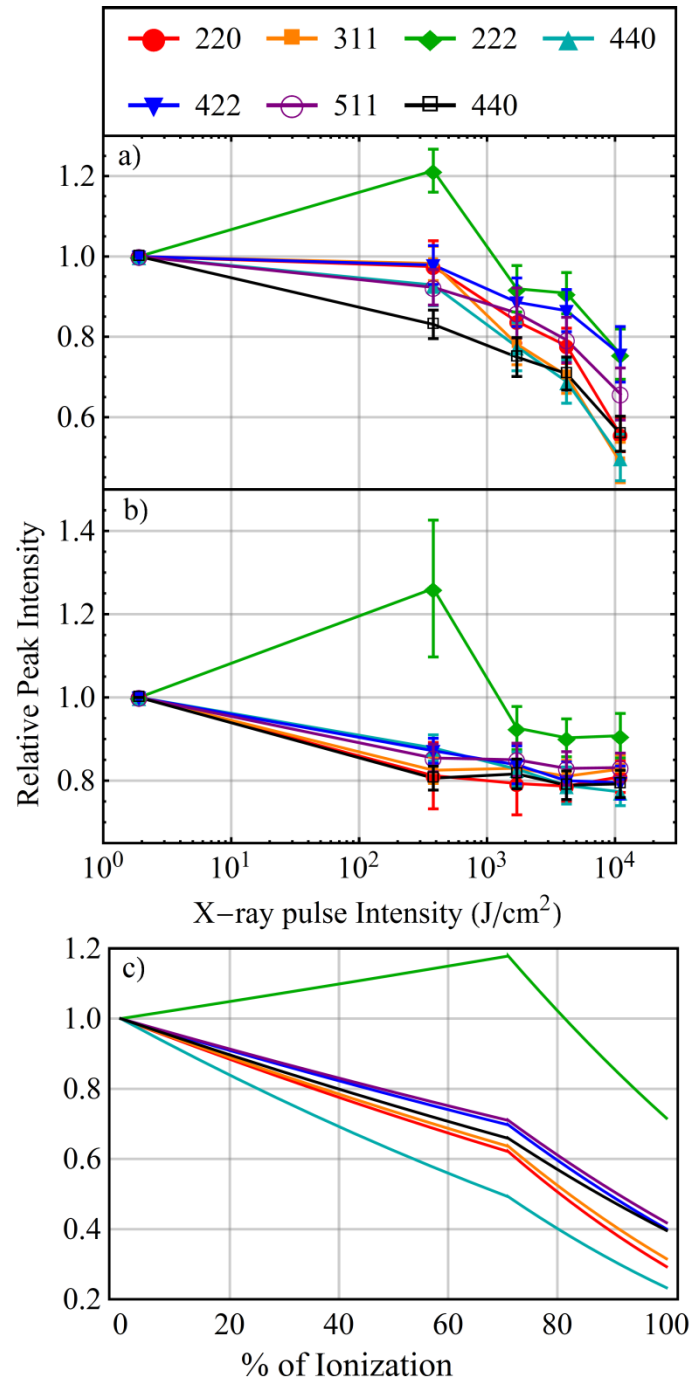


Figure 3.5: Same data as Fig. 3.4 plotted against Bragg angle and compared with the Debye-Waller factor for several values of RMS atomic displacement. (cite fe3o4 paper in preparation)

